

1 EMS Measurement of the Valence Spectral Function of Silicon - a test of Many-body Theory

C. Bowles, A.S. Kheifets, V.A. Sashin, M. Vos, E. Weigold¹

Atomic and Molecular Physics Laboratories, Research School of Physical Sciences and Engineering, Australian National University, Canberra, 0200 Australia

F. Aryasetiawan

Research Institute for Computational Sciences, AIST, Tsukuba Central 2, Umezono 1-1-1, Tsukuba Ibaraki 305-8568 Japan

1.1 Introduction

The electronic properties of the ground states of semiconductors have been studied both experimentally and theoretically for many years. Thus angle resolved photoelectron spectroscopy (ARPES), especially in combination with tunable synchrotron light sources, has been extensively used to map the dispersion of bands in single crystals. However, in the past the experimental work has concentrated almost exclusively on the measurement of energies, and the theoretical valence-band structure calculations have been tested essentially only in terms of their predictions of eigenvalues. In contrast, relatively little attention has been given to the wave function of the electrons, despite the fact that wave function information provides a much more sensitive way of testing the theoretical model under investigation. Although the wave function cannot be measured directly it is closely related to the spectral momentum density. In the independent particle model it is simply proportional to the modulus square of the one-electron wave function,

$$A(\mathbf{q}, \omega) = \sum_{\mathbf{G}\mathbf{k}} n_{j,\mathbf{k}} |\Phi_{j,\mathbf{q}}(\mathbf{q})|^2 \delta(\mathbf{q} - \mathbf{k} - \mathbf{G}) \delta(\omega - \varepsilon_{j\mathbf{k}}), \quad (1.1)$$

where $\Phi(\mathbf{q})$ is the momentum-space one-electron wave function, j is the band index, \mathbf{k} the crystal wave vector, and $n_{j\mathbf{k}}$ and $\varepsilon_{j\mathbf{k}}$ are the occupation number and energy of the corresponding one-electron state. The reciprocal lattice vector \mathbf{G} translates the momentum \mathbf{q} to the first Brillouin zone. For an interacting many-electron system the full spectral electron momentum density (SEMD) is given by

$$A(\mathbf{q}, \omega) = \frac{1}{\pi} G^-(\mathbf{q}, \omega) = \frac{1}{\pi} \frac{1}{[\omega - h - \Sigma(\mathbf{q}, \omega)]} \quad (1.2)$$

¹e-mail: erich.weigold@anu.edu.au

Here $G^-(\mathbf{q}, \omega)$ is the interacting single-hole (retarded) Green's function of the many-electron system, Σ is the self energy and h is the one-electron operator, which includes the kinetic energy and the Coulomb potential from the nuclei and the average of the electron charge cloud density (the Hartree potential). Presuming that the Green's function can be diagonalized on an appropriate basis of momentum-space quasiparticle states $\phi_j(\mathbf{q})$ (e.g. orbitals in atoms, Bloch waves in crystals) then for a crystal it takes the form [1]

$$A(\mathbf{q}, \omega) = \sum_{j, \mathbf{k}, \mathbf{G}} |\phi_j(\mathbf{q})|^2 \delta_{\mathbf{q}, (\mathbf{k} + \mathbf{G})} \frac{1}{\pi} \text{Im} G_j^-(\mathbf{k}, \omega). \quad (1.3)$$

In the absence of electron-electron interactions the non-interacting Green's function is simply a delta function and eq. (1.3) reduces to eq. (1.2). The interacting SEMD contains much more information than simply the band dispersion. The main feature describes the probability of quasiparticle in band j having momentum \mathbf{k} and energy ω . The center of the quasiparticle peak is shifted with respect to the one-electron energy $\varepsilon_{j\mathbf{k}}$ and it acquires a width due to the finite quasiparticle lifetime. In addition electron correlation effects can give rise to significant satellite structures.

The full SEMD can be measured by electron momentum spectroscopy (EMS) [1, 2], in which the energies E_0 , E_1 and E_2 and momenta \mathbf{k}_0 , \mathbf{k}_1 and \mathbf{k}_2 of the incident (subscript 0) and two outgoing electrons (subscripts 1 and 2) in high-energy high-momentum-transfer ($e, 2e$) ionizing collisions are fully determined. From energy and momentum conservation one can determine for each ($e, 2e$) event the binding (or separation) energy of the ejected electron

$$\omega = E_0 - E_1 - E_2, \quad (1.4)$$

and the recoil momentum of the ionized specimen

$$\mathbf{q} = \mathbf{k}_1 + \mathbf{k}_2 - \mathbf{k}_0. \quad (1.5)$$

The differential cross section is given by [2].

$$\sigma(\mathbf{k}_0, \mathbf{k}_1, \mathbf{k}_2, \omega) = (2\pi)^4 k_0^{-1} k_1 k_2 f_{ee} A(\mathbf{q}, \omega). \quad (1.6)$$

Here f_{ee} is the electron-electron scattering factor, which is constant in the non-coplanar symmetric high-energy ($e, 2e$) kinematics used in the spectrometer at the Australian National University [3, 4]. Thus the ($e, 2e$) cross section is directly proportional to the full interacting SEMD. Since the EMS measurements involve real momenta, the crystal momentum \mathbf{k} not appearing in the expression for the cross section, EMS can measure SEMDs for amorphous and polycrystalline materials as well as for single crystals.

The prototype semiconductor silicon has been used as a test-bed to investigate the influence of electron correlations on the SEMD, $A(\mathbf{q}, \omega)$. Many first-principles calculations have been carried out on bulk silicon, see e.g. refs [5, 6, 7, 8, 9, 10, 11, 12]. The majority of these calculations are based on the *GW* approximation to the interacting Green's function [13, 14]. The dispersion of the bulk bands in silicon has been studied with ARPES along high symmetry directions (see e.g. refs [15, 16, 17]). However, there has been essentially no experimental

data available on the shapes of the quasiparticle peaks (i.e. quasiparticle lifetimes) as a function of momentum, and the satellite density as a function of energy and momentum. These properties of the SEMD arise directly from electron correlation effects and provide stringent tests for approximations to the many-electron problem. First-principles calculations of many physical quantities of interest require the interacting one-particle Green's function as input. It is therefore important to have reliable methods for accurately calculating and testing the real and imaginary parts of the self energy, and hence of $A(\mathbf{q}, \omega)$.

There are severe difficulties in extracting the full $A(\mathbf{q}, \omega)$ from experimental data obtained by other techniques. In ARPES these difficulties include knowing the specifics of the transitions involved, such as the untangling of final-state effects from the initial-state ones, and the strong energy and momentum dependence of the matrix elements [13, 18]. ARPES is also very surface sensitive, which can obscure details of the bulk electronic structure (see e.g. [17]). In addition there is usually a significant background underlying the photo-electron spectrum and this can hide any continuous satellite contributions. Certain Compton scattering experiments in which the struck electron is detected in coincidence with the scattered photon, so-called $(\gamma, e\gamma)$ experiments, can in principle map out the spectral function [19, 20]. However, the energy resolution is such that it is extremely difficult to resolve even the valence contributions from that of the core electrons [21].

In this paper we present EMS measurements of the valence spectral momentum density for the prototypical and most studied semiconductor, silicon, and compare the results with calculations based on the independent particle approximation as well as calculations based on many-body approximations to the interacting one-particle Green's function. In section 1.2 we discuss the experimental technique. The theoretical models are outlined in section 1.3. The results are discussed and compared with the FP-LMTO calculations and the first-principles many-body calculations in section 1.4 and, where appropriate, with previous ARPES data. In section 1.4 the role of diffraction is also discussed and in the last section a brief summary and conclusion is given.

1.2 Experimental Details

An outline of the experimental apparatus (described fully in [3, 4]) and the coordinate system is shown in Fig. 1.1. An electron gun emits a highly collimated 25 keV electron beam, which enters the sample region inside a hemisphere held at +25 kV. Thus 50 keV electrons impinge on the target sample along the z -direction, the diameter of the beam being 0.1 mm. The emerging pairs of electrons with energies near 25 keV are decelerated and focussed at the entrance of two symmetrically mounted hemispherical electrostatic analyzers. The analyzers detect electrons emerging along sections of a cone defined by $\Theta_s = 44.3^\circ$, which is chosen so that if all three electrons are in the same plane then there is no momentum transferred to the target (i.e. $q = 0$). In the independent particle picture this corresponds to scattering from a stationary electron. If the electrons are not in the same plane (i.e. $\phi_1 \neq \phi_2$) then there is a y -component of momentum with $q_x = q_z = 0$, that is only target electrons with momentum \mathbf{q} directed along the y -axis can cause a coincidence event. The electrons are detected by two-dimensional position-sensitive electron detectors, mounted at the exit planes of the analyzers, which measure simultaneously over a range of energies and y -momenta (i.e. range of angles

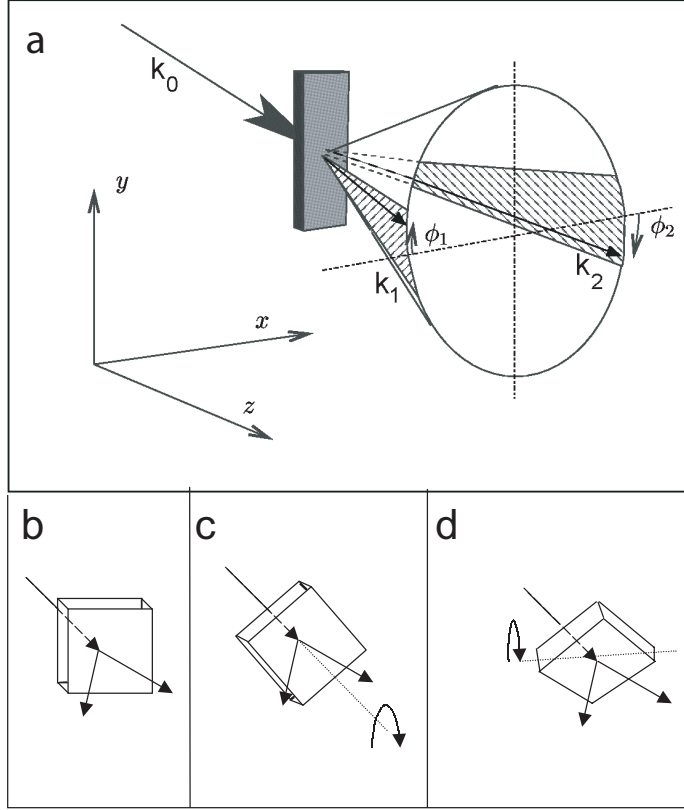


Figure 1.1: Schematics of the experimental arrangements. Incident electrons of momentum k_0 along the z -axis eject an electron from a thin self-supporting Si crystal. The scattered and ejected electrons emerging along the shaded portions of the cone defined by $\Theta = 44.3^\circ$, are detected in coincidence by two energy and angle sensitive analysers. In the bottom panels the sample is indicated as a block with sides parallel to the $\langle 010 \rangle$ and $\langle 001 \rangle$ symmetry directions. Thus in (b) the spectral momentum density is measured along the $\langle 010 \rangle$ direction. In (c) the density is measured along the $\langle 110 \rangle$ direction, as the crystal has been rotated about the surface normal by 45° . In (d) the crystal has been tilted by 35.3° relative to the position in (c) so that the density is measured along the $\langle 111 \rangle$ direction.

ϕ).

Two pairs of deflection plates mounted inside the high-voltage hemisphere along the sections of the cone can be used to change the effective scattering angle by up to 1° . In this way [3] one can select nonzero values for the x - and/or the z -component of momentum, the y -component always lying in the range 0-5 a.u. (atomic units are used here, 1 a.u. = 1.89 \AA^{-1}). This allows one to probe the full three-dimensional momentum space. The two double deflectors are also used to check that the measured momenta correspond to the expected ones [3, 22], ensuring that there are no offsets in q_x or q_z as a result of any small possi-

ble geometrical misalignments. The orientation of the target specimen can be determined by observing the diffraction pattern of the transmitted electron beam on a phosphorus screen. A specific direction of the thin crystal target is then aligned with the y -axis of the spectrometer so that we measure the energy-resolved momentum density along that direction. The sample orientation can be changed without removing the sample from the vacuum by means of the manipulator mounting arrangement [3].

The single crystal target has to be an extremely thin self-supporting film. The initial part of the target preparation followed the procedure of Utteridge et al [23]. First a buried silicon oxide layer was produced by ion implantation in a crystal with $\langle 100 \rangle$ surface normal. A crater was then formed on the back of the crystal by wet chemical etching. The oxide layer serves to stop the etching. It is then removed by a HF dip and the sample is transferred to the vacuum. At this stage the thickness of the thinned part of the crystal is around 200 nm. Low energy (600 eV) argon sputtering is then used to further thin the sample. The thin part of the crystal is completely transparent. The thickness is monitored by observing the colour of the transmitted light from an incandescent lamp placed behind the sample. The colour changes with thickness due to the interference of the directly transmitted light with that reflected from the front and back silicon-vacuum interfaces. The thinning is stopped when the thickness reaches 20 nm (corresponding to a grey-greenish light). The sample is then transferred to the spectrometer under UHV. A thin amorphous layer could be present on the backside due to the sputtering, whereas the front side (facing the analyzers) is probably hydrogen terminated as a result of the HF dip. The base pressure in the sputtering chamber was of the order of 10^{-9} Torr and in the spectrometer the operating pressure was 2×10^{-10} Torr.

The experimental energy and momentum resolutions were discussed in detail by Vos et al [1]. The full width at half-maximum (FWHM) energy resolution is 1.0 eV, whereas the FWHM momentum resolutions are estimated to be (0.12, 0.10, 0.10 a.u.) for the q_x, q_y, q_z momentum components respectively.

Even for a very thin target multiple scattering by the incoming or outgoing electrons has to be taken into account. These fast electrons can loose energy by inelastic collisions, such as plasmon excitation, or transfer momentum by elastic collisions (deflection from the nuclei). These scattering events move real coincident ($e, 2e$) events to "wrong" parts of the spectrum, as either the energy or momentum conservation equations (eqs. 1.4 and 1.5) are used incorrectly. For polycrystalline or amorphous solids these multiple-scattering events can be modeled by Monte Carlo simulations [24]. In the case of inelastic scattering the binding energy as inferred from eq. 1.4 will be too high. Inelastic multiple scattering events can be deconvoluted from the data by measuring an energy loss spectrum for 25 keV electrons passing through the sample. This deconvolution is done without using any free parameters [25]. This approach is used in the present case. Figure 1.2 shows the energy loss spectrum obtained with the present silicon crystal target. For single crystals elastic scattering from the nuclei adds up coherently (diffraction). The change of the incoming or outgoing momenta by diffraction changes the outcome of the measurement by a reciprocal lattice vector. We demonstrate later in this paper how different measurements can be used to disentangle the diffracted contributions from the primary (non-diffracted) contribution.

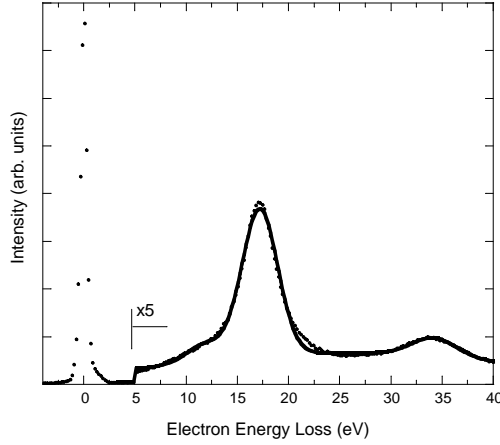


Figure 1.2: The energy loss spectrum observed in the spectrometer for the 20 nm thick Si crystal sample with 25 keV incident electrons. The fitted curve is used to deconvolute the data for inelastic scattering.

1.3 Theory

1.3.1 Independent Particle Approximation

The local density approximation (LDA) of density functional theory (DFT) has long been established as a very useful tool for investigating ground-state properties of bulk semiconductors from first principles [26, 27]. The advantage of DFT for approximate calculations in many-body systems is that one extracts the needed information from a one-body quantity, the electron density $n(\mathbf{r})$. Although the one-particle eigenvalues in the theory have no formal justification as quasiparticle energies, in practice they turn out to be surprisingly accurate [28].

We employed here the linear-muffin-tin-orbital (LMTO) method [29] within the framework of DFT. The LMTO method is just one of many computational schemes derived within the framework of the DFT. The great practical advantage of the LMTO method is that only a minimal basis set of energy-independent orbitals (typically 9-16 per atom) is needed to obtain accurate eigenvalues (band energies). In the present study we implemented a full-potential version (FP-LMTO) of the method [30]. We write the one-electron wave function in a crystal in the tight-binding representation as the Bloch sum of the localised MT orbitals:

$$\Psi_{jk}(\mathbf{r}) = \sum_{\mathbf{t}} e^{i\mathbf{k}\cdot\mathbf{t}} \sum_{\Lambda} a_{\Lambda}^{jk} \phi_{\Lambda}(\mathbf{r} - \mathbf{R} - \mathbf{t}). \quad (1.7)$$

Here \mathbf{k} is the crystal momentum, j band index, \mathbf{t} lattice (translation) vector and \mathbf{R} basis vector. The label Λ defines a MT orbital centered at a given site \mathbf{R} and it comprises the site index \mathbf{R} and a set of atomic-like quantum numbers. The expansion coefficients a_{Λ}^{jk} are found by solving the eigenvalue problem using the standard variational technique.

Momentum space representation of the wave function Ψ_{jk} is given by the Fourier trans-

form of the Bloch function:

$$\Phi_{j\mathbf{k}}(\mathbf{q}) = \int e^{-i\mathbf{q}\cdot\mathbf{r}} \Psi_{j\mathbf{k}}(\mathbf{r}) d\mathbf{r}. \quad (1.8)$$

Due to the periodic nature of the charge density the only non-zero contributions to $\Phi_{j\mathbf{k}}(\mathbf{q})$ occur when $\mathbf{q} = \mathbf{k} + \mathbf{G}$ with \mathbf{G} a reciprocal lattice vector.

$$\Phi_{j\mathbf{k}}(\mathbf{q}) = \sum_{\mathbf{G}} c_{\mathbf{G},\mathbf{k}}^j \delta(\mathbf{q} - \mathbf{k} - \mathbf{G}). \quad (1.9)$$

The contributions $c_{\mathbf{G},\mathbf{k}}^j$, the Bloch wave amplitudes, are expressed through the (Fourier) integrals:

$$\begin{aligned} c_{\mathbf{G},\mathbf{k}}^j &= \Omega^{-1} \int e^{-i(\mathbf{k}+\mathbf{G})\cdot\mathbf{r}} \Psi_{j\mathbf{k}}(\mathbf{r}) d\mathbf{r} \\ &= \Omega^{-1} \sum_{\Lambda} [a_{\Lambda}^{j\mathbf{k}} e^{-i(\mathbf{k}+\mathbf{G})\cdot\mathbf{R}} \int e^{-i(\mathbf{k}+\mathbf{G})\cdot\mathbf{r}} \phi_{\Lambda}(\mathbf{r}) d\mathbf{r}] \end{aligned} \quad (1.10)$$

Here it is assumed that the wave function $\Psi_{j\mathbf{k}}$ is normalized in the unit cell of the volume Ω . The limits of the three-dimensional integration indicates symbolically the whole coordinate space. The EMD in the occupied part of the band j is proportional to the modulus squared Bloch amplitudes:

$$\rho_j(\mathbf{q}) = \frac{\Omega^2}{(2\pi)^3} \sum_{\mathbf{G}} n_{j\mathbf{k}} |\Phi_j(\mathbf{k} + \mathbf{G})|^2 \delta_{\mathbf{q},\mathbf{k}+\mathbf{G}} \quad (1.11)$$

where $n_{j\mathbf{k}}$ is the occupation number. The EMD (1.11) is normalized to the total number of valence electrons per unit cell:

$$2 \sum_j \int d\mathbf{q} \rho_j(\mathbf{q}) = n_e. \quad (1.12)$$

1.3.2 Electron Correlation Models

The hole Green's function entering equation 1.3 can be calculated by the many-body perturbation theory (MBPT) expansion on the Bloch wave basis (1.7). Taking the first non-vanishing term in the MBPT leads to the so-called *GW* approximation [31, 32]. In this acronym *G* stands for the Green's function and *W* denotes the screened Coulomb interaction. The *GW* approximation is known to give accurate quasiparticle energies [14]. However, its description of satellite structures is not satisfactory. In alkali metals, for example, photoemission spectra show the presence of multiple plasmon satellites whereas the *GW* approximation yields only one at too large an energy. This shortcoming of the *GW* approximation has been resolved by introducing vertex corrections in the form of the cumulant expansion to the Green's function [33, 34, 35]. This allowed the inclusion of multiple plasmon creation. As a result the calculated peak positions of the plasmon satellites were found to be in much better agreement with the experiment than those predicted by the *GW* scheme itself [36, 37, 38].

Formally, the cumulant expansion for the one-hole Green's function can be derived as follows. We choose the time representation for the Green's function, drop the band index j for brevity, and write it as

$$G(\mathbf{k}, t < 0) = i\theta(-t)e^{-i\omega_k t + C^h(\mathbf{k}, t)}, \quad (1.13)$$

where ω_k is the one-electron energy and $C^h(\mathbf{k}, t)$ is defined to be the cumulant. Expanding the exponential in powers of the cumulant we get

$$G(\mathbf{k}, t) = G_0(\mathbf{k}, t) \left[1 + C^h(\mathbf{k}, t) + \frac{1}{2} [C^h(\mathbf{k}, t)]^2 + \dots \right], \quad (1.14)$$

where $G_0(\mathbf{k}, t) = i\theta(-t) \exp(-i\omega_k t)$. In terms of the self-energy Σ , the Green function for the hole can be expanded as

$$G = G_0 + G_0 \Sigma G_0 + G_0 \Sigma G_0 \Sigma G_0 + \dots \quad (1.15)$$

To lowest order in screened interaction W , the cumulant is obtained by equating

$$G_0 C^h = G_0 \Sigma G_0, \quad (1.16)$$

where $\Sigma = \Sigma_{GW} = iG_0 W$. The first-order cumulant is therefore

$$C^h(\mathbf{k}, t) = i \int_t^\infty dt' \int_{t'}^\infty d\tau e^{i\omega_k \tau} \Sigma(\mathbf{k}, t). \quad (1.17)$$

This is then put back into Eq. (1.13) yielding multiple plasmon satellites. The energy-momentum representation of the Green's function can be restored by the time Fourier transform.

1.4 Results and Discussions

1.4.1 Band Structure

We first discuss the dispersion $\varepsilon_{j\mathbf{k}}(\mathbf{q})$, i.e. the dependence of the energy of the Bloch function $\Phi_{j\mathbf{k}}(\mathbf{q})$ of band j on its crystal momentum $\mathbf{k} = \mathbf{q} + \mathbf{G}$. The band with the largest binding energy is labeled 1, the next one 2 etc. In momentum space the Bloch function with crystal momentum \mathbf{k} is non-zero only at momentum values $\mathbf{k} + \mathbf{G}$ with amplitude $c_{\mathbf{G},\mathbf{k}}^j$ (see eq. 1.9).

The band structure and momentum densities obtained by Kheifets et al. [30] in a FP-LMTO calculation (based on the DFT-LDA) are shown in Fig. 1.3, the bands being labeled as discussed above. The bands are periodic in \mathbf{q} space, with band 1 having a maximum in the binding energy at the Γ points. However, the only Γ point with significant momentum density in band 1 is the one corresponding to zero momentum (see lower panel in Fig. 1.3). Thus the function with the lowest energy is a Bloch function with $k = 0$, $c_{(0,0,0),\mathbf{k}}^1 \simeq 1$, and the other $c_{\mathbf{G},\mathbf{k}}^1 \simeq 0$.

The cut of the first four Brillouin zones of silicon along the $q_z = 0$ plane is shown in Fig. 1.4. For a free electron solid the wave functions are plane waves and in the ground state the

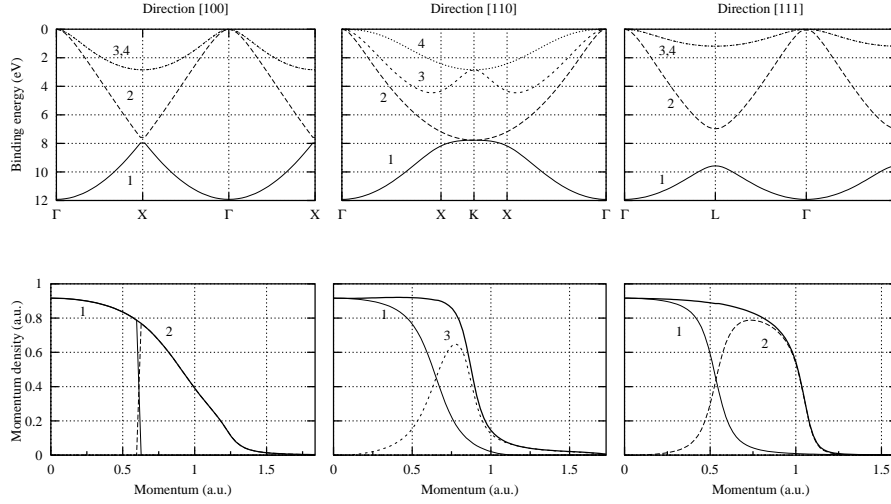


Figure 1.3: FP-LMTO calculations [30] of the dispersion (top panel) and momentum density (bottom panel) of Si for different high symmetry crystallographic directions. The total momentum density is split up into the densities of the individual bands as indicated.

occupied states are within the Fermi sphere with radius k_f i.e. $|k| < k_f$. The intersection of this sphere with the $q_z = 0$ plane is indicated by the dashed circle in Fig. 1.4. The lattice potential of silicon can be viewed as a perturbation on the free electron picture, so that the wave functions are Bloch functions with more than one $|c_{Gk}^j|^2 > 0$. The semiconductor silicon has 8 valence electrons per unit cell, and hence the first 4 bands are fully occupied with one spin up and one spin down electron per band. We will now discuss the results of the measurement of silicon and emphasize that the electron density for band j is at its maximum in Brillouin zone j .

The sample was a thin ($\simeq 20$ nm) single silicon crystal with $\langle 001 \rangle$ surface normal, which is first aligned with the z direction (i.e. aligned with k_0 , see Fig. 1.1 (a)). Rotating around the surface normal, measurements were taken with the sample $\langle 100 \rangle$ direction aligned along the y -axis, then the $\langle 110 \rangle$ direction and 4 intermediate directions were aligned along the y -axis as shown in Fig. 1.4. In all these cases the potentials on the sets of deflector plates were set to ensure that the measurements passed through zero momentum (corresponding to $\Gamma_{(0,0,0)}$). The experimentally observed density distributions, together with the results of the FP-LMTO calculation, are shown in Fig. 1.5 for the 6 directions measured through $\Gamma_{(0,0,0)}$. The calculations were broadened with the experimental 1 eV energy resolution and split up into the 4 occupied bands.

For the measurement of momenta directed along the $\langle 100 \rangle$ direction (0° in Fig. 1.4) the theory predicts bands 1 and 2 occupied. In the first Brillouin zone band 1 is occupied, changing abruptly to band 2 at 0.61 a.u. (see also Fig. 1.4 and left panel of Fig. 1.3). There is no band gap in the dispersion on crossing the first Brillouin zone. This is due to additional symmetry of the diamond lattice (see e.g. [39]). After leaving the second Brillouin zone the

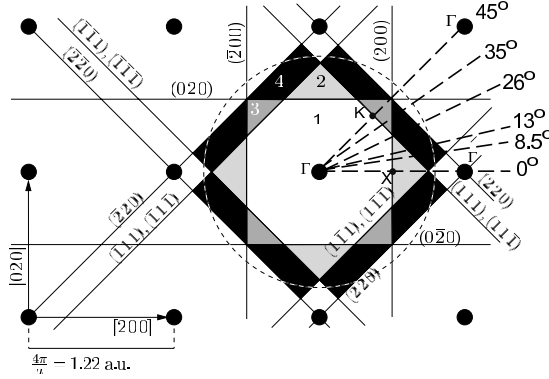


Figure 1.4: The cut through the reciprocal lattice of silicon along the $q_z = 0$ plane with the first 4 Brillouin zones labeled. The Brillouin zone boundaries are labeled by the indices of the reciprocal lattice it bisects. The Brillouin zone is bisected by the Fermi sphere for a free electron solid with the same electron density as silicon. Different measurements through the $q = 0$ point are indicated by the dashed lines.

calculated density drops only gradually to zero. The measured density (left panel of Fig. 1.5) has the same behaviour, but also shows an additional branch at smaller binding energies, which merges with the main feature at 1.2 a.u. This additional branch can also be seen in the calculated band structure for the case where the crystal has been rotated by 8.5° , and comes from band 4. From the shape of the Brillouin zone shown in Fig. 1.4 it is clear that the measurement along the $\langle 100 \rangle$ direction just misses Brillouin zone 4. Due to finite momentum resolution it is obvious that the measurement will pick up contributions from this zone, giving rise to the extra branch in the observed intensity.

In the $\langle 110 \rangle$ symmetry direction (reached by a rotation by 45° along the surface normal) the first Brillouin zone crossing is two planes, (the (111) and $(11\bar{1})$ planes), making an angle of $\pm 54.35^\circ$ with the $q_z = 0$ plane. Thus the band switches from 1 to 3 at the double crossing. This gives rise to the classic band gap behaviour, band 1 having a minimum in binding energy (maximum in energy) at the Brillouin zone crossing, with its density petering out after the crossing. Band 3 slowly increases in intensity from zero momentum up to the first Brillouin zone boundary, where it has a maximum in binding energy, with increased density as one passes through Brillouin zone 3. The next extremum in energy, which corresponds to a minimum in binding energy, is when band 3 crosses the next set of Brillouin zone boundaries, i.e. on leaving Brillouin zone 3, and its intensity decreases thereafter as the momentum increases. The calculations and measurements are in quite good agreement with each other for these general features. For the intermediate angles band 1 remains dominant, band 4 is prominent, band 2 makes a significant contribution for directions not far from the $\langle 100 \rangle$ direction, and band 3 make small contributions close to the $\langle 110 \rangle$ direction.

Also shown in Fig. 1.5 (bottom panels) is the spectral momentum density obtained along the $\langle 111 \rangle$ direction. This direction was reached by tilting the $\langle 110 \rangle$ aligned sample over 35.3° (see Fig. 1.1(d)). Here the density is due to bands 1 and 2 with a large band gap at the

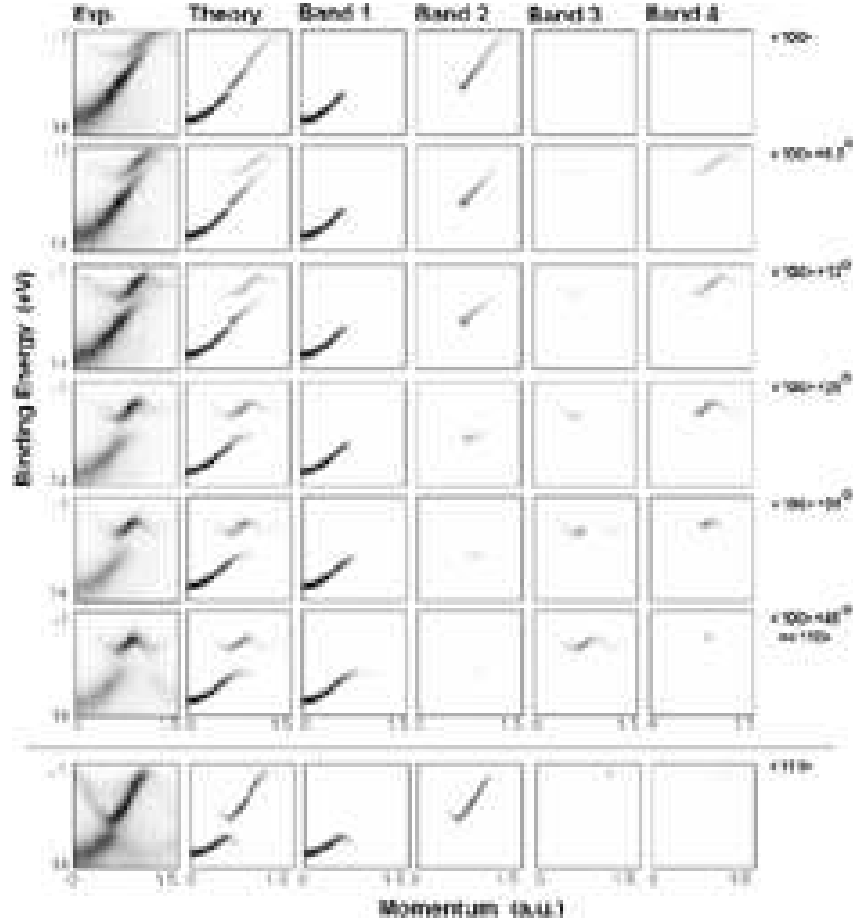


Figure 1.5: The LMTO calculated spectral momentum densities (total plus separate band contributions) along the directions shown in Fig. 1.4 compared with the measured results. The calculations have been broadened by the experimental energy resolution. The bottom panel shows the results along the $\langle 111 \rangle$ direction.

zone crossing. Again these general features of the experiment and theory are in reasonable agreement. Note that the dispersion in the $\langle 111 \rangle$ direction could be mapped over a much larger momentum range than expected based on the momentum density distribution (see Fig. 1.3 bottom panel). This is due to diffraction, as is described later.

A more detailed comparison between the calculated and measured dispersion of the bands in the three high symmetry directions is shown in Fig. 1.6. Here a fitting procedure was used to extract the peak position of the measured density at different momenta. For comparison we include for the $\langle 100 \rangle$ and $\langle 111 \rangle$ directions also the ARPES data of refs. [16] and [17]. The agreement between the calculation and the present measurement is excellent. There is a small

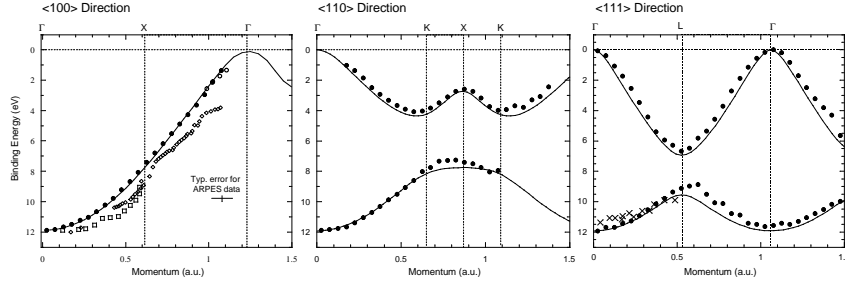


Figure 1.6: The measured dispersion in the peak density (dots) along the $\langle 100 \rangle$ (left panel), $\langle 110 \rangle$ (central) and $\langle 111 \rangle$ (right panel) symmetry directions. The full line is the LMTO calculation. Only those branches of the band structure are shown that are expected to have non-zero intensity in the EMS measurement. The open circles are ARPES data from ref. [16] and the diamonds, squares and crosses are ARPES data from [17].

deviation near the X -point in the $\langle 110 \rangle$ direction, with the observed gap between bands 1 and 3 being a little smaller than given by theory. A similar deviations for the band gaps is observed near the L points in the $\langle 111 \rangle$ direction. Generally the EMS shapes are smoother and better defined than the ARPES ones.

Fig. 1.7 shows the band structures measured with the $\langle 110 \rangle$ direction aligned with the y -axis at three different values of q_x , i.e. 0, 0.65 a.u., and 0.87 a.u., the latter two being along Brillouin zone boundaries. The offsets in the x -component of momentum are produced by choosing suitable settings for the deflector voltages for each set of deflectors [22]. For the measurement with $q_x = q_z = 0$, there is a single dispersing feature with a band gap at $q_y = 0.65$ a.u. due to the crossing of the zone boundary. This momentum value corresponds to a K point of the band structure. Since the x - and y -directions through the Γ point are equivalent, the binding energy spectra at the two K points, $(q_x, q_y, q_z) = (0, 0.65, 0)$ and $(0.65, 0, 0)$, should be identical. This is indeed the case [22].

The total band width can be obtained from the zero momentum spectrum of the measurement along the $\langle 111 \rangle$ direction. Here both the top and the bottom of the band are clearly visible. The experimental separation between the two peaks is 11.85 ± 0.2 eV. The error is mainly due to the uncertainty in the shape of the background under the high-binding energy peak. The LMTO calculation gives a value of 11.93 eV.

As an alternative way of determining the valence band width we measured the valence band and Si 2p core level in the same experiment. This allows us to determine precisely the position of the valence band bottom relative to the $2p_{3/2}$ component of the core line. The fit result gives a value of 86.65 ± 0.2 eV for their energy separation. From photoemission data (e.g.[40]) we know that the $2p_{3/2}$ binding energy relative to the valence band maximum is 98.74 eV. In this way we obtain a value of 12.1 ± 0.2 eV for the valence band width.

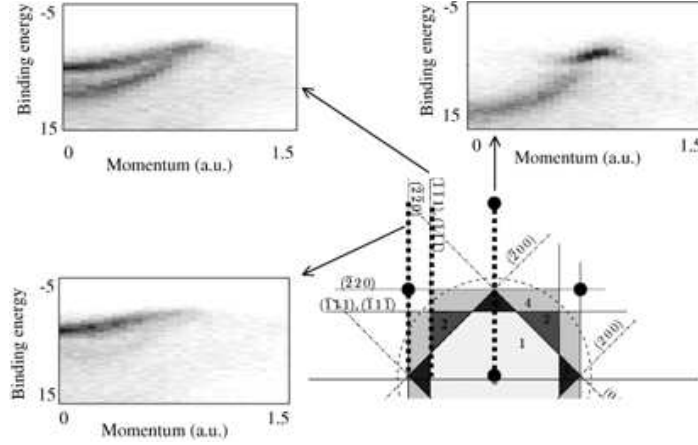


Figure 1.7: The measured densities along the lines indicated in the Brillouin zone cut. The x -axis of the spectrometer coincides with the crystal $\langle 1\bar{1}0 \rangle$ direction. One line goes through the Γ point (zero momentum), one has a constant q_x component of 0.65 a.u. and one has a constant q_x component of 0.87 a.u. The latter two lines coincide with Brillouin zone edges.

1.4.2 Diffraction Effects

In a crystal coherent elastic scattering by the nuclear sites (dynamic diffraction) of the incident and/or the emitted electrons can shift the observed momentum distribution by a reciprocal lattice vector \mathbf{G} [41, 42, 43]. In the present experiment the electron momenta are all very large ($k_0 = 62.1$ a.u., $k_{1,2} = 43.4$ a.u.), so that for the dominant diffraction the vectors \mathbf{G}_i are all much smaller than the respective \mathbf{k}_i . Thus the \mathbf{G}_i must be essentially perpendicular to the \mathbf{k}_i vector to fulfil the diffraction condition $2\mathbf{k}_i \cdot \mathbf{G}_i + G_i^2 = 0$. In the case where the surface normal (the $\langle 100 \rangle$ direction) is aligned with \mathbf{k}_0 the smallest \mathbf{G}_0 contributing to diffraction are of type $\langle \pm 2 \pm 2 0 \rangle$ (see ref. [41] for a detailed discussion). The smallest vector \mathbf{q} that can be accessed is 1.22 a.u. where the density is very low (see Fig. 1.3), and it appears at $q_y = 1.22$ a.u. Diffraction events of the type $\langle 0 \pm 4 0 \rangle$ produce an offset in the y -component of momentum by 2.44 a.u. The measured y -momentum line still passes through the origin so that we can still measure electrons with $q = 0$. Thus this diffracted beam causes a weak replication of the main spectrum shifted by 2.44 a.u. For the outgoing electrons the diffraction depends on which crystal direction is aligned with the y -axis of the spectrometer [41].

In the apparatus it is possible to rotate the sample about the y -axis. This does not affect the direction of measurement, but it does affect the directions of the incoming and outgoing electrons relative to the crystal symmetry directions and hence their diffraction. In general, rotating away from the symmetric configuration, there will be fewer small reciprocal lattice vectors that can contribute to diffraction, decreasing their influence. However, such a rotation cannot eliminate the contributions from reciprocal lattice vectors of the type $\langle 0 \pm 2 0 \rangle$, which are perpendicular to the incoming and outgoing beams.

In Fig. 1.8 we show the measured energy resolved momentum densities for two high symmetry directions in a grey-scale plot with the LMTO band structure in the repeated zone

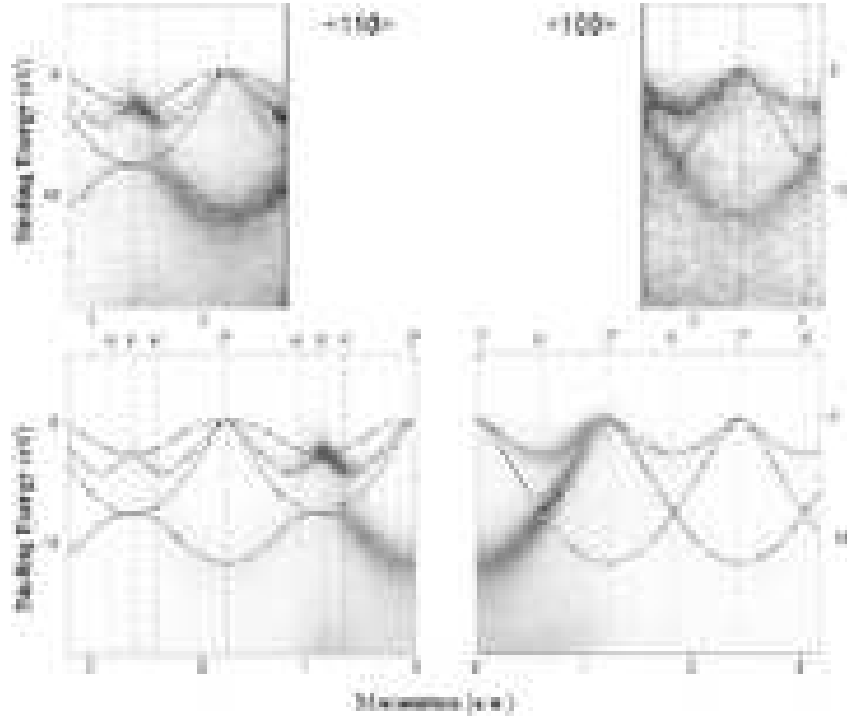


Figure 1.8: Measured momentum densities along the $\langle 110 \rangle$ (left) and $\langle 100 \rangle$ (right) directions in linear grey-scale with the LMTO band structure in the repeated zone scheme superimposed. The top panels show the high momentum parts with an enhanced grey-scale to highlight the low intensity diffracted contributions.

scheme superimposed on it. The contributions due to diffracted beams can be seen particularly at large momentum in the top panels with their enhanced grey-scale. At $q = 0$ the two spectral densities should be identical, however, as can be seen from the figure, at this Γ point there is a small peak in the density close to zero binding energy in the $\langle 100 \rangle$ direction, which is absent in the $\langle 110 \rangle$ direction. This density is due to the $\langle 111 \rangle$ reciprocal lattice vector (the shortest reciprocal lattice vector for the diamond lattice, length 1.06 a.u.) shifting density from $\Gamma_{(1,1,1)}$ to $\Gamma_{(1,0,0)}$. Rotation by 10° around the spectrometer y -axis removes this peak at low binding energies [41]. In this way, by examining the diffracted contributions in regions where the spectral density should be zero, it is possible to remove the diffracted components from the measured spectral momentum density. This is shown explicitly in Fig. 1.9.

Diffraction effects are most obvious when the $\langle 111 \rangle$ direction is aligned with the spectrometer y -axis as can be seen already in the bottom panel of Fig. 1.5. The measured intensity distribution is given by the crosses in Fig. 1.9, which shows cuts through the data at the indicated binding energies. At the valence band maximum there are five peaks visible, at $q = 0$, ± 1.05 a.u., and ± 2.1 a.u. The dominant peaks at ± 1.05 a.u. are due to momentum density at the top of band 2 (see Fig. 1.3), the other peaks are due to diffraction by a crystal reciprocal

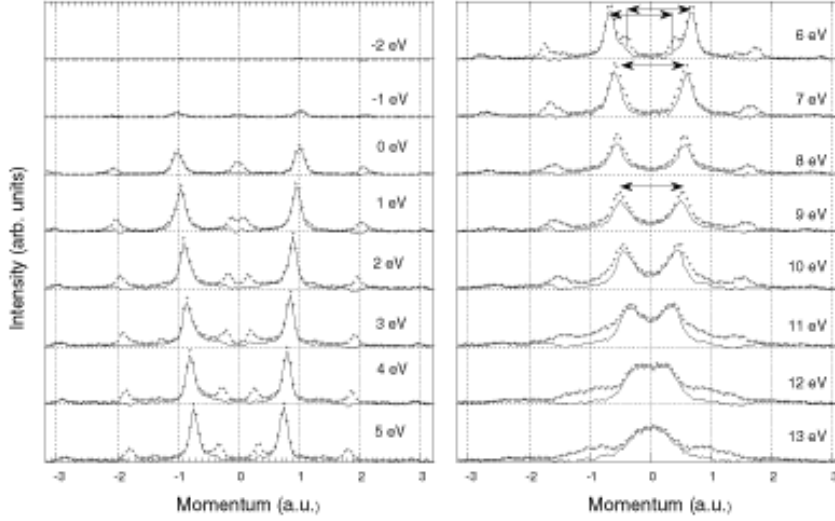


Figure 1.9: The measured intensities (crosses) along $\langle 111 \rangle$ direction. The solid lines give the momentum densities corrected for diffraction as discussed in the text. In the right panel the length of the reciprocal lattice vector $\mathbf{G} = \langle 111 \rangle$ is indicated as well.

lattice vector. By assuming that the diffracted components add incoherently to the real spectral momentum density, the latter can be obtained by subtraction. The resulting momentum density is indicated by the solid line in Fig. 1.9. The small gap between bands 1 and 2 (see Fig. 1.3) shows up as a reduction in density around 8 eV.

After subtraction of the diffracted component the peak at the top of the valence band at $\mathbf{q} = 0$ disappears completely, indicating that it was entirely due to diffraction with a reciprocal lattice vector of either $\mathbf{G} = \langle 111 \rangle$ or $\mathbf{G} = \langle -1 - 1 - 1 \rangle$. However, in the binding energy range near 6 eV there are clear shoulders left after subtraction. This is to be expected as near the Brillouin zone boundary these plane waves are expected to contribute significantly to the Bloch waves. The shoulder and main line that are part of the same Bloch function are shown in this figure, connected by a line of the length of the reciprocal lattice vector.

1.4.3 Many-body Effects

Up to this point we have concentrated on those aspects of the electronic structure of silicon that could be understood in the independent particle picture. However, even from the semi-quantitative grey-scale presentations in Fig. 1.5 (and Fig. 1.8) of the measured intensities it is clear that they do not follow the LMTO calculations in detail. The measurements show maximum intensity at intermediate energies or near the top of the band, whereas the theory predicts maximum intensity near the bottom of the band. Also the energy-widths of the measured density distributions at a given momentum are much larger than the theoretical ones even though the experimental energy resolution has been included in the calculations. This is due to lifetime broadening of the spectral momentum density by electron correlation effects.

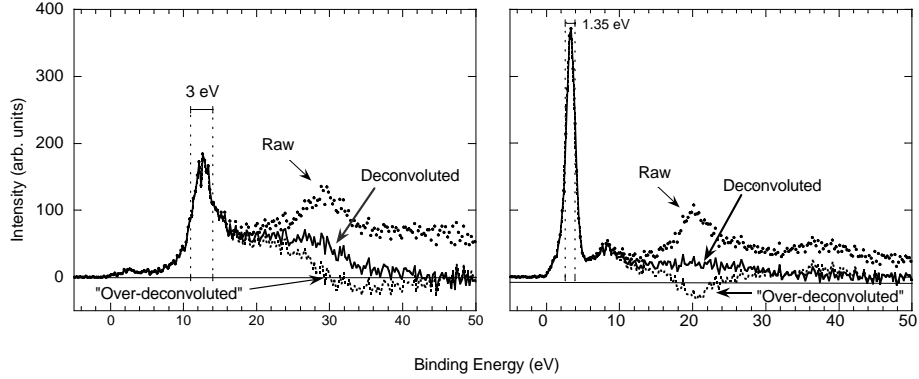


Figure 1.10: EMS spectra along the $\langle 110 \rangle$ direction at $q_y \simeq 0$ near the Γ point (left) and $q_y \simeq 0.87$ a.u. near the X point (right). An identical deconvolution procedure is followed for both spectra. The raw data are indicated by the dots, the data deconvoluted for inelastic multiple-scattering contributions by the solid line, and the squares show data that have deliberately been ‘over-deconvoluted’ (see text for details).

We will now look at some binding energy spectra at appropriate momenta in more detail in order to explore the role of many-body effects in the electronic structure of silicon.

Fig. 1.10 shows two spectra obtained along the $\langle 110 \rangle$ direction, one at $q \simeq 0$ near the Γ point and the other at $q \simeq 0.87$ a.u. near the X point. The peak near the X point is very much narrower and taller than the peak near $q \simeq 0$. The latter is also quite asymmetric. As well as the raw data the figure includes a curve showing the data deconvoluted, in a parameter-free way, for inelastic scattering using only the measured energy loss spectrum (see Fig.1.2) [1]. This still leaves considerable intensity at high binding energies, extending some 20 eV or more above the position of the quasiparticle peak. If one tries to remove all the intensity at binding energies above the quasiparticle peak by further deconvolution one obtains non-physical negative intensities at some binding energies.

In order to describe the data more quantitatively we performed full-scale many-body calculations using the GW and Cumulant Expansion approximations to the one-hole Green’s function (see section 1.3.2). The results are presented in Fig 1.11, which shows raw as well as the deconvoluted spectra along each of the two symmetry directions compared with the first-principles many-body calculations. The theories, convoluted with the experimental energy resolution, are normalized to the data at one point only, namely to the peak of the quasiparticle structure in the common $q \simeq 0$ spectra, the theories having the same total density in these spectra. The small low binding energy peak present in the data in the $\langle 100 \rangle$ direction at intermediate q_y values and not in the calculations is due to the picking up of intensity from band 4 as discussed earlier.

The GW calculation gives a peak in the satellite intensity at around 34 eV at $\mathbf{q} \simeq 0$. This is not observed in the data. This is a well-known failure of the GW approximation [13]. The cumulant expansion calculation gives a better fit to the data, although it too gives

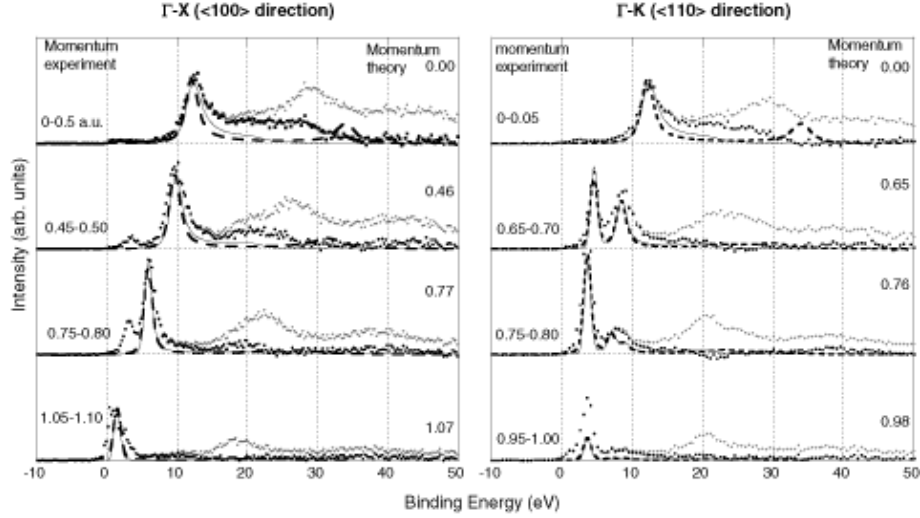


Figure 1.11: EMS spectra, raw and deconvoluted for inelastic multiple-scattering effects, at selected momenta along the $\langle 100 \rangle$ (top) and $\langle 110 \rangle$ (bottom) directions. The full and dashed lines are the results of the cumulant expansion and GW calculations, respectively, and they are normalized to the quasiparticle peak at $q = 0$.

smaller satellite density than the experiment. Both calculations describe the main quasiparticle features quite well in all the spectra. In particular they give the broadening and the asymmetric structure of this feature reasonably accurately at the smaller momenta. It is this broadening which gives rise to the reduction in the peak heights at the lower momenta. However, even though the calculations give significant life-time broadening, they nevertheless underestimate the width of the quasiparticle structure, the cumulant expansion model giving a slightly better fit.

The finite quasiparticle (hole) lifetimes causes broadening of the observed features. In Fig. 1.12 we plot as a function of the momentum the observed width (FWHM) for spectra obtained along the $\langle 100 \rangle$ direction. Near zero momentum the binding energy is a weak function of momentum, and the observed width should be a good indication of the life-time broadening. Away from zero momentum the binding energy becomes a strong function of momentum, and additional broadening is observed due to the finite momentum resolution of the spectrometer as initial states with slightly different momenta (and hence binding energy) contribute to the spectra. In spite of this a decrease in width is observed with increasing momentum. The sharpest spectra are observed where the dispersion goes again through an extremum (now minimum binding energy) i.e. near the X point ($\langle 100 \rangle$ direction, see also fig. 1.10) and the L point ($\langle 111 \rangle$ direction). Here a width of 1.35 eV is observed, a width clearly dominated by the energy resolution of the spectrometer. Also shown in the figure are the FWHM given by the many-body calculations. At zero momentum the calculated width is significantly smaller than the observed width (even if the calculations are broadened with the spectrometer energy

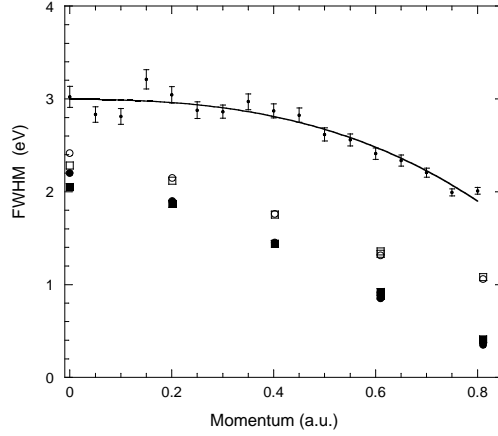


Figure 1.12: The FWHM of the quasiparticle peaks in the $\langle 100 \rangle$ direction plotted as a function of momentum. The measurements are indicated by the points with error bars. The thin line is a smooth fit to the experimentally obtained FWHM. The theoretical estimate of the peak width is indicated by squares (*GW* theory) and circles (cumulant expansion theory). The filled symbols refer to the calculated line width whereas the open symbols include the effect of finite experimental energy resolution.

resolution). The calculated width decreases more rapidly with momentum, which is, at least in part, due to the fact that we did not incorporate the effects of finite energy and momentum resolution in the calculations.

The density of the quasiparticle structure and the total density along the $\langle 100 \rangle$ direction are plotted in fig. 1.13. Also shown are the quasi-particle densities given by the cumulant expansion calculations, which somewhat underestimate the satellite density. For this figure the satellite density was defined as the total density above the main quasi-particle feature, whereas in the experiment we take the intensity extending 20 eV above the end of the quasi-particle peak. In this way we obtain for the experiment that the percentage of the total density that is contained in the satellite structure decreases as the momentum increases. For instance, along the $\langle 100 \rangle$ direction, the satellite structure has essentially disappeared by momentum values near 1 a.u., whereas at $\mathbf{q} = 0$ it accounts for around 40 % of the total density (Fig. 1.13). In the theory the satellite intensity remains fairly constant (at 25 % of the total density) but becomes more spread out over binding energy with increasing momentum.

1.5 Conclusions

We have measured the spectral momentum density of the prototype semiconductor Si along the three high symmetry directions, and several cuts between the $\langle 100 \rangle$ and $\langle 110 \rangle$ directions, all going through zero momentum (the $\Gamma_{(0,0,0)}$ point). In addition several measurements were made along the $\langle 110 \rangle$ direction but with the cuts shifted from $\Gamma_{(0,0,0)}$ point to coincide with nearby Brillouin zone edges.

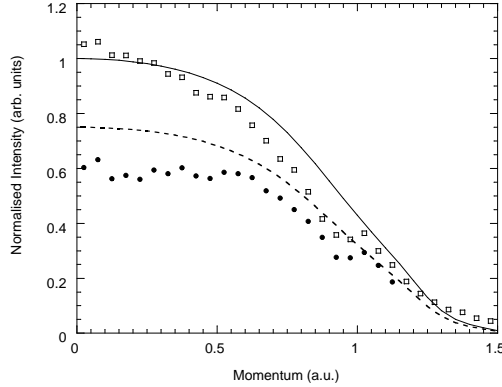


Figure 1.13: The energy integrated electron momentum density along the $\langle 100 \rangle$ direction. The open squares give the total density, and the solid circles the quasi-particle density. Also included is the total density given by the LMTO calculation (solid line) and the corresponding quasi-particle intensity, as predicted by the cumulant expansion calculations (dashed line).

The band structure, i.e. the dispersion of the position of the peak in the quasiparticle structure, is very well described by the FP-LMTO-DFT-LDA approximation. The present EMS data are in better agreement with the theory than the available ARPES data. The band-width was determined to be 11.85 ± 0.2 eV, in good agreement with ARPES data (12.5 ± 0.6 eV [44]) and the LMTO theory (11.93 eV).

Diffraction of the incident and/or the emitted electron beams can shift intensity from the ‘direct’ spectral density by reciprocal lattice vectors. Such effects are observed but can often be distinguished from the ‘direct’ intensity. Changing the diffraction conditions for the incoming and/or outgoing electrons pinpoints which part of the measured intensity is diffraction related. In this way contributions due to diffraction can be removed on the assumption that there is no interference between the direct and diffracted electron waves. The study of any possible interference effects could lead to additional information on the structure of silicon [41].

The spectra, especially at low momenta, show very large effects due to correlations. In particular the quasiparticle structures are very broad due to the short hole lifetimes, and much of the spectral density is found in higher energy satellite structure. This satellite structure is quite smooth and extends to around 20 eV above the quasiparticle peak. Although the satellite structure dominates the density at low momentum, its density drops off as the momentum is increased. Similarly the lifetime broadening diminishes as the momentum increases. Comparison with first principles many-body calculations shows that the *GW* approximation predicts the main quasiparticle features reasonably well, but cannot describe the satellite structure. The cumulant expansion approximation also describes the quasiparticle features qualitatively well, but does considerably better than the *GW* in its description of the shape of the satellite density. Although it predicts the energy distribution and the momentum dependence of the satellite structure quite well, it nevertheless significantly underestimates the satellite intensity, particularly at low momenta. The fact that agreement is better but still not perfect for the more

detailed model is encouraging in that a quantitative comparison between the present EMS data and other representations of the many-body wave function should lead to new levels of understanding.

1.6 Acknowledgements

We are grateful to the Australian Research Council for financial support.

Bibliography

- [1] M. Vos, A. S. Kheifets, V. A. Sashin, E. Weigold, M. Usuda, and F. Aryasetiawan. Quantitative measurement of the spectral function of aluminum and lithium by electron momentum spectroscopy. *Phys. Rev. B*, 66:155414, 2002.
- [2] E. Weigold and I. E. McCarthy. *Electron Momentum Spectroscopy*. Kluwer Academic/Plenum, New York, 1999.
- [3] M. Vos, G. P. Cornish, and E. Weigold. A high-energy ($e,2e$) spectrometer for the study of the spectral momentum density of materials. *Rev. Sci. Instrum.*, 71:3831–3840, 2000.
- [4] M. Vos and E. Weigold. Developments in the measurement of spectral momentum densities with ($e,2e$) spectrometers. *J. Electron Spectrosc. Relat. Phenom.*, 112:93–106, 2000.
- [5] A. Fleszar and W. Hanke. Spectral properties of quasiparticles in a semiconductor. *Phys. Rev. B*, 56:10228–10232, 1997.
- [6] A.S. Kheifets and Y.Q. Cai. Energy-resolved electron momentum densities of diamond-structure semiconductors. *J. Phys.: Condens. Matter*, 7:1821–1833, 1995.
- [7] W. Borrmann and P. Fulde. Exchange and correlation effects of the quasiparticle band structure of semiconductors. *Phys. Rev. B*, 35:9569–9579, 1987.
- [8] K. Sturm, W. Schülke, and J. R. Schmitz. Plasmon-Fano resonance inside the particle-hole excitation spectrum of simple metals and semiconductors. *Phys. Rev. Lett*, 68:228–231, 1992.
- [9] M. S. Hybertsen and S. G. Louie. Electron correlation in semiconductors and insulators: Band gaps and quasiparticle energies. *Phys. Rev. B*, 34:5390–5413, 1986.
- [10] R. W. Godby, M. Schlüter, and L. J. Sham. Self-energy operators and exchange-correlation potentials in semiconductors. *Phys. Rev. B*, 37:10159–10175, 1988.
- [11] M. Rohlfing, P. Krüger, and J. Pollmann. Quasiparticle band-structure calculations for C, Si, Ge, GaAs, and SiC using gaussian-orbital basis sets. *Phys. Rev. B*, 48:17791–17805, 1993.
- [12] G. E. Engel and W. E. Pickett. Investigation of density functionals to predict both ground-state properties and band structures. *Phys. Rev. B*, 54:8420–8429, 1996.
- [13] L. Hedin. On correlation effects in electron spectroscopies and the GW approximation. *J. Phys: Condens. Matter*, 11:R489–R528, 1999.
- [14] F. Aryasetiawan and O. Gunnarsson. The GW method. *Rep. Prog. Phys.*, 61:237, 1998.
- [15] L. S. O. Johansson, P. E. S. Persson, U. O. Karlsson, and R. I. G. Uhrberg. Bulk electronic structure of silicon studied with angle-resolved photoemission from the Si(100) 2×1 surface. *Phys. Rev. B*, 42:8991–8999, 1990.

- [16] A. L. Wachs, T. Miller, T. C. Hsieh, A. P. Shapiro, and T.-C. Chiang. Angle-resolved photoemission studies of Ge(111)-c(2x8), Ge(111)-(1x1)H, Si(111)-(7x7) and Si(100)-(2x1). *Phys. Rev. B*, 32:2326–2333, 1985.
- [17] D. H. Rich, G. E. Franklin, F. M. Leibsle, T. Miller, and T. C. Chiang. Synchrotron photoemission studies of the Sb-passivated Si surfaces: Degenerate doping and bulk band dispersion. *Phys. Rev. B*, 40:11804–11816, 1989.
- [18] A. Bansil, M. Lindroos, S. Sahrakorpi, R. S. Markiewicz, G. D. Gu, J. Avila, L. Roca, A. Tejada, and M. C. Asensio. First principles simulations of energy and polarization dependent angle-resolved photoemission spectra of Bi2212. *J. Phys. Chem. Solids*, 63:2175–2180, 2002.
- [19] F. Bell and J. R. Schneider. Three-dimensional electron momentum densities of solids. *J. Phys.: Condens. Matter*, 13:7905–7922, 2001.
- [20] T. Sattler, Th. Tschentscher, J. R. Schneider, M. Vos, A. S. Kheifets, D. R. Lun, E. Weigold, G. Dollinger, H. Bross, and F. Bell. The anisotropy of the electron momentum density of graphite studied by $(\gamma, e\gamma)$ and $(e, 2e)$ spectroscopy. *Phys. Rev. B*, 63:155204, 2001.
- [21] M. Itou, S. Kishimoto, H. Kawata, M. Ozaki, H. Sakurai, and F. Itoh. Three-dimensional electron momentum density of graphite by (x, ex) spectroscopy with a time of flight electron energy spectrometer. *J. Phys. Soc. Japan*, 68:515, 1999.
- [22] M. Vos, V. A. Sashin, C. Bowles, A. S. Kheifets, and E. Weigold. Probing the spectral densities over the full three-dimensional momentum space. *J. Phys. Chem. Solids*, in press, 2004.
- [23] S. J. Utteridge, V. A. Sashin, S. A. Canney, M. J. Ford, Z. Fang, D. R. Oliver, M. Vos, and E. Weigold. Preparation of a 10 nm thick single-crystal silicon membrane self-supporting over a diameter of 1 mm. *Appl. Surf. Sci.*, 162-163:359–367, 2000.
- [24] M. Vos and M. Bottema. Monte Carlo simulations of $(e, 2e)$ experiments in solids. *Phys. Rev. B*, 54:5946–5954, 1996.
- [25] M. Vos, A. S. Kheifets, and E. Weigold. Electron momentum spectroscopy of metals. In D. H. Madison and M. Schulz, editors, *Correlations, Polarization and Ionization in Atomic Systems, IAP Conference Proceedings 604*, pages 70–75, New York, 2002. American Institute of Physics.
- [26] R.O. Jones and O. Gunnarsson. The density functional formalism, its applications and prospects. *Rev. Mod. Phys.*, 61:689–746, 1989.
- [27] R.M. Dreizler and E.K.U. Gross. *Density Functional Theory*. Springer Verlag, Berlin, 1990.
- [28] W.E. Pickett. Electronic structure of the high-temperature oxide superconductors. *Rev. Mod. Phys.*, 61:433–512, 1989.
- [29] H.L. Skriver. *The LMTO Method*. Springer Verlag, Berlin, 1984.
- [30] A. S. Kheifets, D. R. Lun, and S. Yu Savrasov. Full-potential linear-muffin-tin-orbital calculation of electron momentum densities. *J. Phys.: Condens. Matter*, 11:6779–6792, 1999.
- [31] L. Hedin. Method for calculating the one-particle green’s function with application to the electron-gas problem. *Phys. Rev.*, 139:A796–A823, 1965.

- [32] L. Hedin and S. Lundqvist. *Solid State Physics*, 23:1–181, 1969.
- [33] D. C. Langreth. Singularities in x-ray spectra of metals. *Phys. Rev. B*, 1:471, 1970.
- [34] B. Bergersen, F. W. Klus, and C. Blomberg. Single particle Green's function in the electron-plasmon approximation. *Can.J.Phys.*, 51:102, 1973.
- [35] L. Hedin. Effects of recoil on shake-up spectra in metals. *Physica Scripta*, 21:477–480, 1980.
- [36] F. Aryasetiawan, L. Hedin, and K. Karlsson. Multiple plasmon satellites in Na and Al spectral functions from ab initio cumulant expansion. *Phys. Rev. Lett.*, 77:2268–2271, 1996.
- [37] M. Vos, A. S. Kheifets, E. Weigold, S. A. Canney, B. Holm, F. Aryasetiawan, and K. Karlsson. Determination of the energy-momentum densities of aluminium by electron momentum spectroscopy. *J. Phys.: Condens. Matter*, 11:3645, 1999.
- [38] M. Vos, A. S. Kheifets, and E. Weigold. The spectral momentum density of aluminum measured by electron momentum spectroscopy. *J. Phys. Chem. Solids*, 62:2215–2221, 2001.
- [39] V. Heine. *Group Theory in Quantum Mechanics*. Pergamonn, New York, 1960.
- [40] F.J. Himpsel, G. Hollinger, and R.A. Pollak. Determination of the fermi-level pinning position at si(111) surfaces. *Phys. Rev. B*, 28:7014–7018, 1983.
- [41] M. Vos, A. S. Kheifets, V. A. Sashin, and E. Weigold. Influence of electron diffraction on measured energy-resolved momentum densities in single-crystalline silicon. *J. Phys Chem. Solids*, 64:2507–2515, 2003.
- [42] L. J. Allen, I. E. McCarthy, V. W. Maslen, and C. J. Rossouw. Effects of diffraction on the (e,2e) reaction in crystals. *Aust. J. Phys.*, 43:453–464, 1990.
- [43] R.S. Matthews. PhD thesis, Flinders University of South Australia, 1993.
- [44] W.D. Grobman and D.E. Eastman. Photoemission valence-band densities of states for si, ge, and GaAs using synchrotron radiation. *Phys. Rev. Lett.*, 29:1508–1512, 1972.